Table S1. Classification of sites from which δ¹⁸O records have been used to infer paleoaltimetry (see Section 4.2 and Figure 15 for more explanation).

5

Site	Latitude (° N)	Longitude (° E)	Paleoaltimetry Studies

Sites that are judged appropriate for δ¹⁸O-paleoaltimetry under high-elevation scenarios (black dots in Fig. 15)

Site	Latitude (° N)	Longitude (° E)	Paleoaltimetry Studies
Gyirong	28.7	85.3	Wang et al. 1996
Hongtupo	31.4	103.5	Xu et al. 2016
Linzhou Basin	30.0	91.2	Ding et al. 2014
Markam Basin	29.7	98.5	Li et al. 2015
Mount Everest	28.3	87.6	Rowley et al. 2001
Namling-Oiyug Basin	29.7	89.5	Currie et al. 2005
Penbo Basin	29.8	91.2	Ingalls et al. 2017

Sites in the southernmost Himalayas where elevations are too low (red dots in Fig. 15)

Site	Latitude (° N)	Longitude (° E)	Paleoaltimetry Studies
Chake Basin	23.8	103.1	Hoke et al. 2014
Eryuan	26.2	99.8	Hoke et al. 2014
Jianchuan Basin	26.6	99.8	Hoke et al. 2014
Lanping	26.5	99.4	Hoke et al. 2014
Luhe	25.2	101.3	Hoke et al. 2014
Nepal Siwaliks	27.4	82.8	Quade et al. 1995
Xiaolongtan Basin	23.6	103.2	Li et al. 2015
Yanyuan	27.5	101.5	Hoke et al. 2014

Sites in northern Tibet (orange dots in Fig. 15)

Site	Latitude (° N)	Longitude (° E)	Paleoaltimetry Studies
Aertashi	38.0	75.6	Kent-Corson et al. 2009
Ganchaigou	37.7	91.0	Kent-Corson et al. 2009
Hexi Corridor	39.5	97.5	Kent-Corson et al. 2009
Huaitoutala	37.3	96.7	Zhuang et al. 2011
Huatugou	38.3	91.8	Li et al. 2016
Janggalsay	38.2	86.6	Kent-Corson et al. 2009
Lake Mahai	37.7	94.2	Kent-Corson et al. 2009

Lao Mangnai	36.9	92.0	Kent-Corson et al. 2009
Lenghu	37.8	93.4	Kent-Corson et al. 2009
Lulehe	37.5	95.1	Kent-Corson et al. 2009
Miran River	39.0	88.9	Kent-Corson et al. 2009
Oytag	39.0	75.5	Bershaw et al. 2011
Puska	37.1	78.6	Kent-Corson et al. 2009
Xiao Qaidam	37.0	94.9	Kent-Corson et al. 2009
Xorkol	39.0	91.9	Kent-Corson et al. 2009

Sites in the western or transitional regions (blue dots in Fig. 15)

India Siwaliks	30.4	77.6	Ghosh et al. 2004
India Siwaliks	30.3	77.6	Sanyal et al. 2005
Kailas Basin	31.2	81.0	DeCelles et al. 2011
Pakistan Siwaliks	33.4	73.1	Quade et al. 1995
Thakkhola	28.7	83.5	Garzione et al. 2000
Thakkhola-Tetang	28.7	83.5	Garzione et al. 2000
Zhada Basin	31.5	79.8	Saylor et al. 2009

Sites in central Tibet (green dots in Fig. 15)

|			
Chaoyang-Hoh Xil Basin	35.5	87.4	Li et al. 2018
Deyu-Hoh Xil Basin	35.7	87.4	Li et al. 2018
Erdagou-Hoh Xil Basin	34.5	92.7	Li et al. 2018
Erdaogou-Hoh Xil Basin	35.0	92.3	Li et al. 2018
Gerze Basin	31.9	85.1	Wei et al. 2016
Hoh Xil Basin	34.6	93.0	Cyr et al. 2005
Kunlun Pass Basin	35.6	94.1	Wang et al. 2008
Linxia Basin	35.7	103.1	Dettman et al. 2003
Lunpola Basin	32.1	89.8	Rowley and Currie 2006
Nima Basin	31.8	87.5	DeCelles et al. 2011
Xuehuan-Hoh Xil Basin	35.1	88.1	Li et al. 2018
Xunhua Basin	35.9	102.5	Hough et al. 2010
Zhuonai-Hoh Xil Basin	35.4	91.8	Li et al. 2018
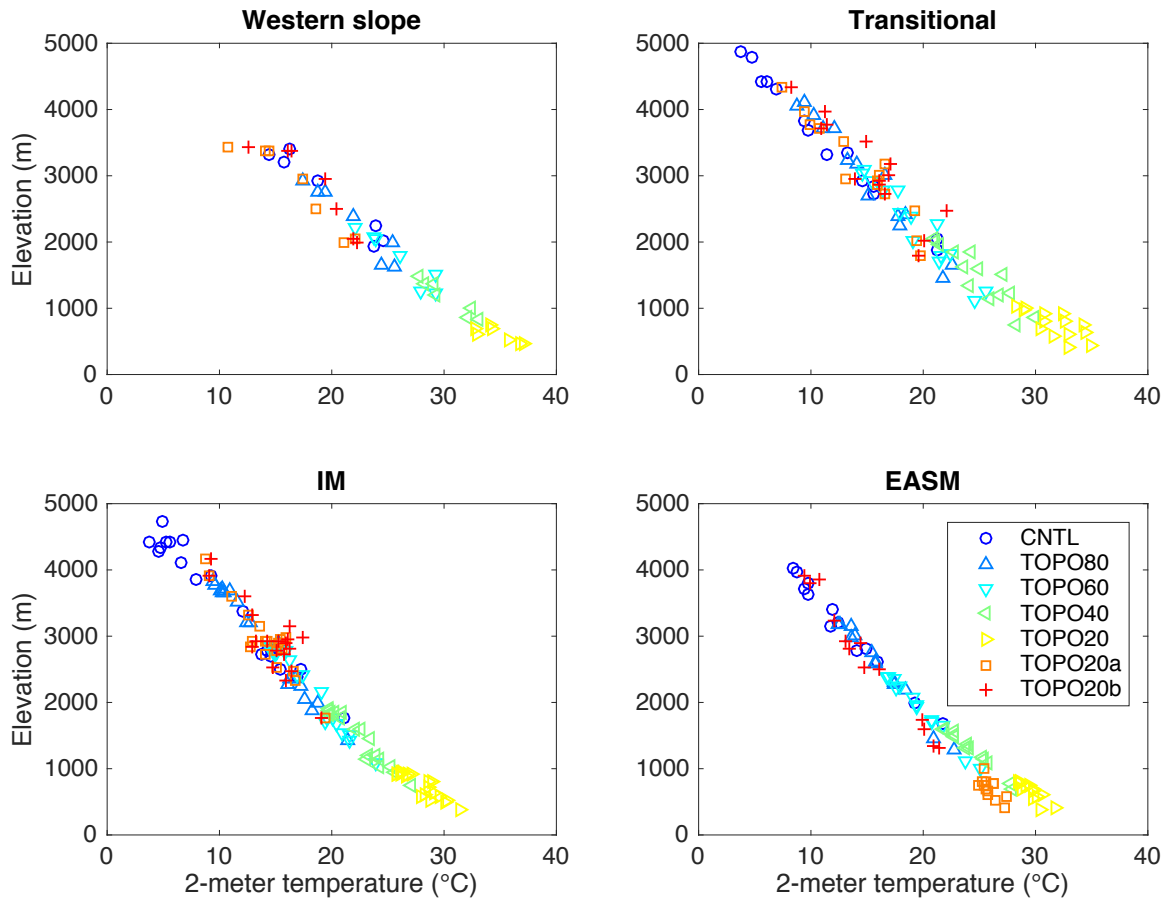
Figure S1. ECHAM5 simulated 2-meter air temperature (°C) versus elevation (m) for (a) western; (b) transitional; (c) IM region; and (c) EASM regions. The symbols indicate the elevation scenarios. Note that when calculating lapse rates using the data in these figures as described in section 3.1, we excluded TOPO40 and TOPO20 in the EASM region, and TOPO20 for the Himalayan and IM domains, since temperature exhibits little relationship with elevation in these low-relief cases.
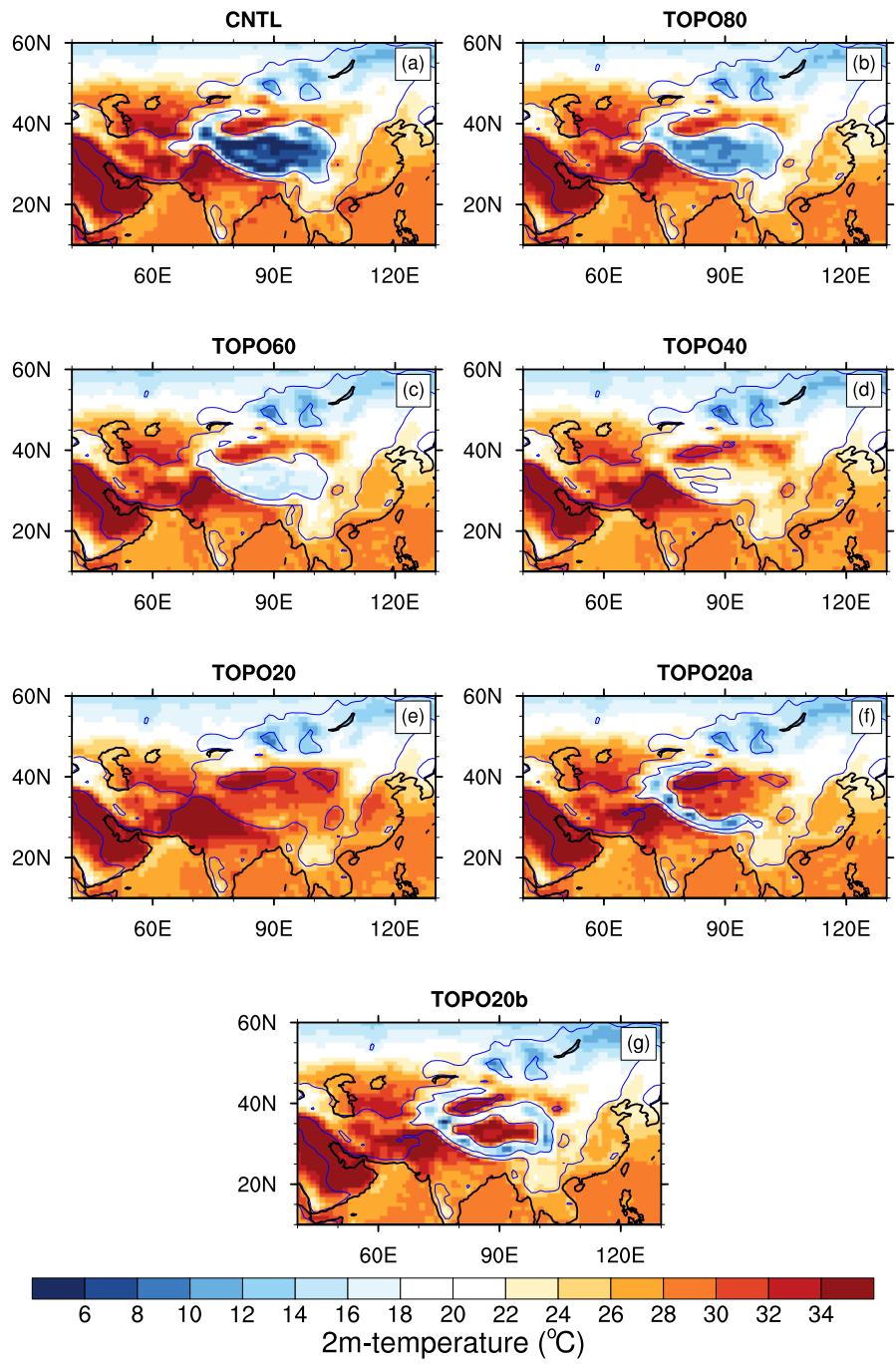
3

Figure S2. ECHAM5 June-July-August 2-meter near surface temperature (°C) for (a) CNTL, (b) TOPO80, (c) TOPO60, (d) TOPO40, (e) TOPO20, (f) TOPO20a, and (g) TOPO20b cases. Blue contour lines mark the 500 and 2000 m Tibetan surface elevations. Temperature decreases on the slope of the Himalayas but remains largely unchanged on the Tibetan Plateau.
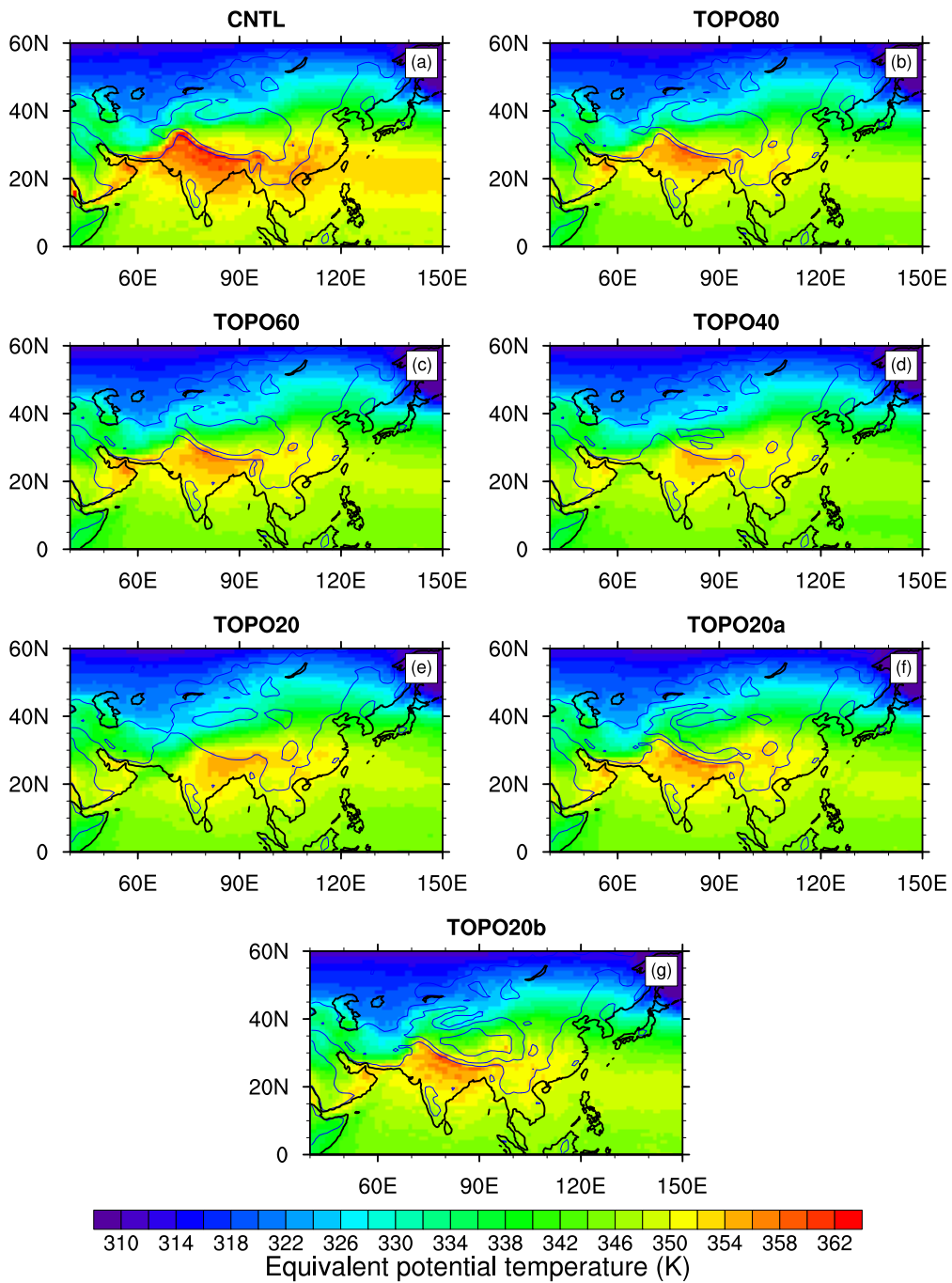
Figure S3. Equivalent potential temperature (K) at the 40 hPa sigma level for (a) CNTL, (b) TOPO80, (c) TOPO60, (d) TOPO40, (e) TOPO20, (f) TOPO20a, and (g) TOPO20b cases. Light blue contours mark 500 m and 2000 m surface elevation contours in the Tibetan reach for each case.
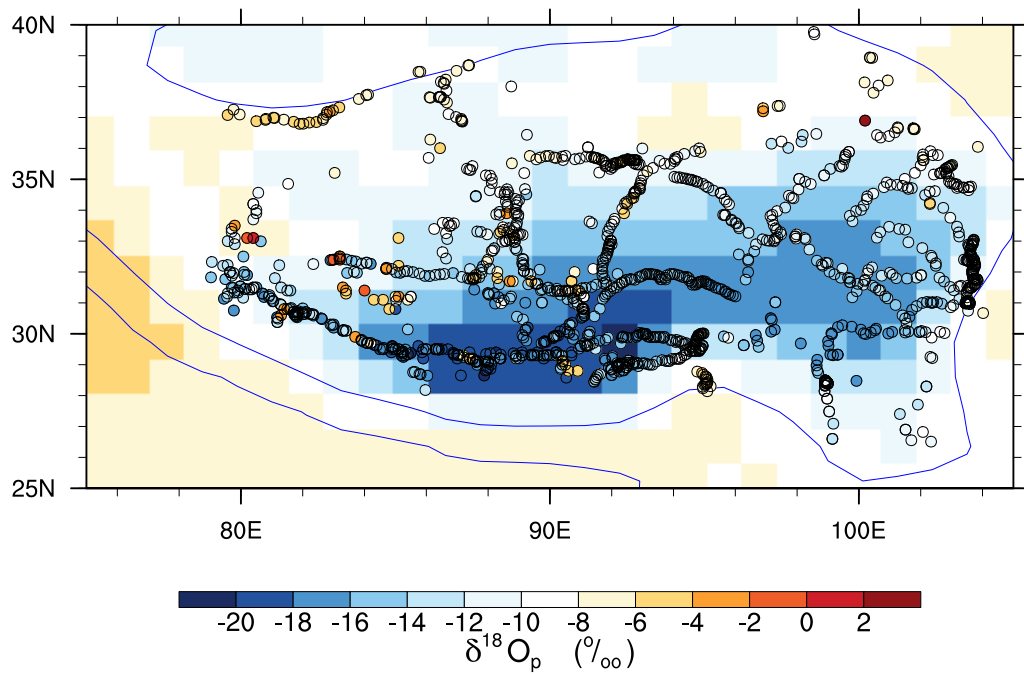
Figure S4. Comparison of Monthly-precipitation-weighted ECHAM δ^{18}O$_p$ (shaded) with precipitation and stream samples (circles) from Li and Garzione (2016).
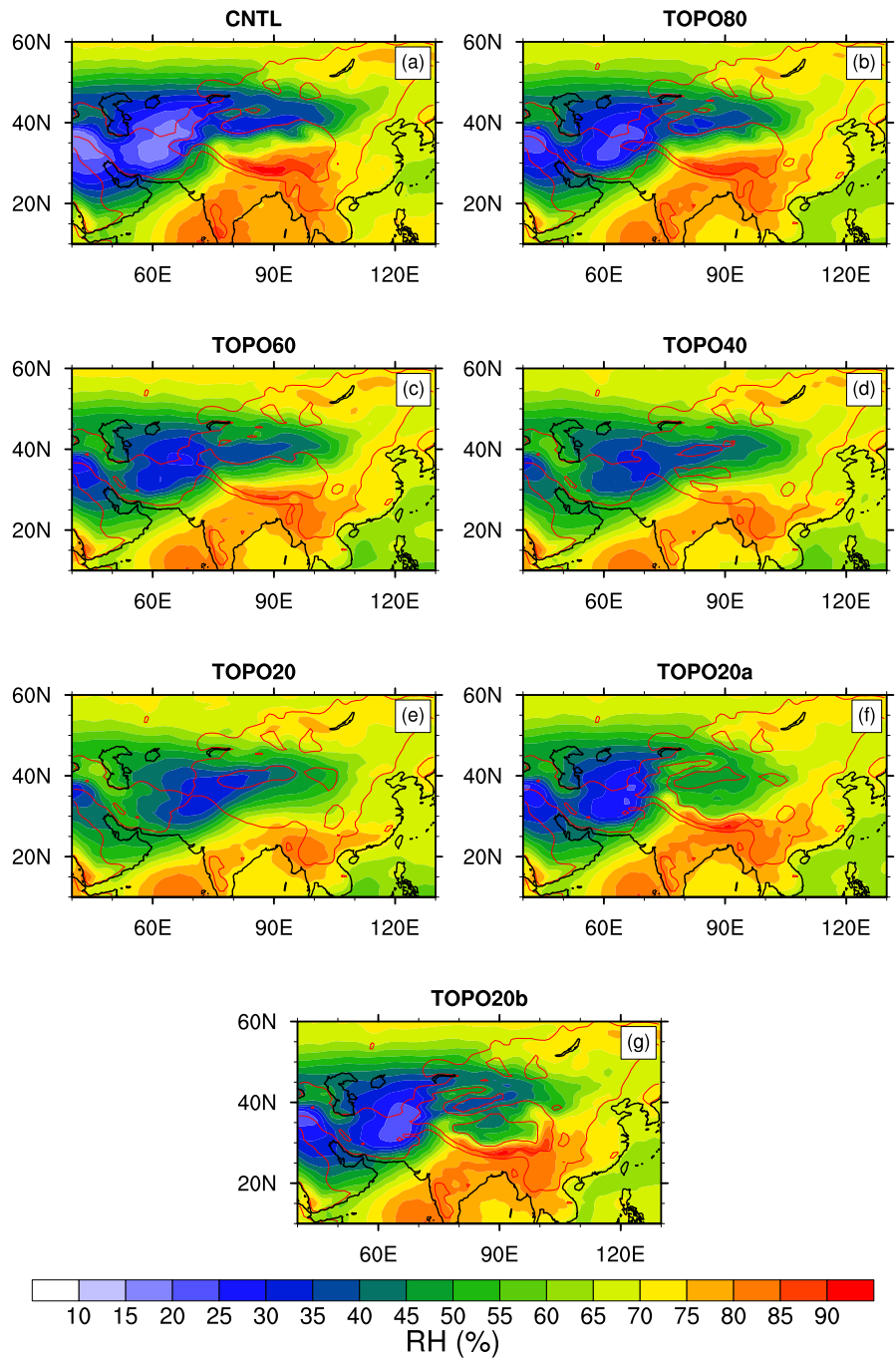
Figure S5. Summer (June-July-August) total-column-averaged relative humidity (shaded) for (a) CNTL (b) TOPO80, (c) TOPO60, (d) TOPO40, (e) TOPO20, (f) TOPO20a, and (g) TOPO20b cases. The red lines mark 500 m and 2000 m surface elevation contours in the Tibetan region.

5
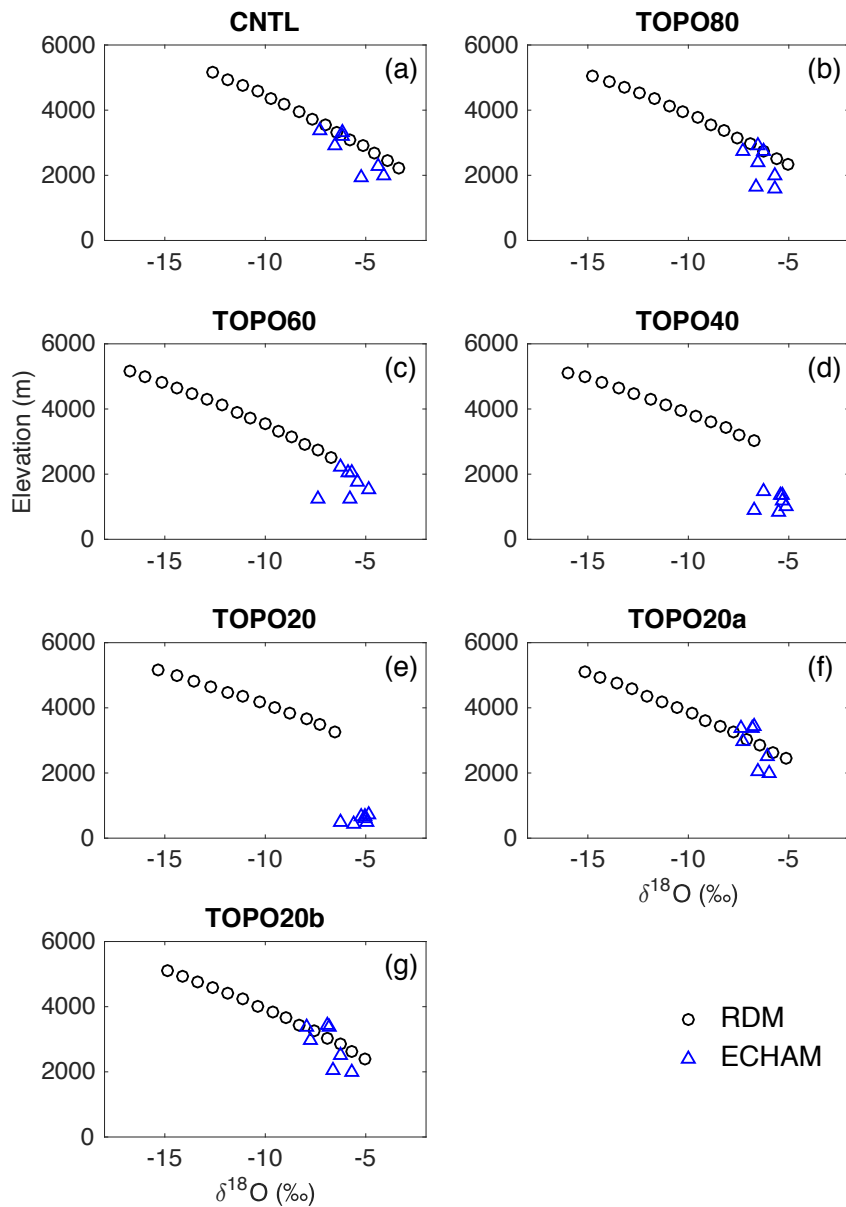
Figure S6. Monthly-precipitation-weighted ECHAM (blue triangle) and RDM (black circle) $\delta^{18}O_p$ (‰) versus elevation (m) plot for the western part of the southern Himalayan flank for the cases (a) CNTL, (b) TOPO80, (c) TOPO60, (d) TOPO40, (e) TOPO20, (f) TOPO20a, and (g) TOPO20b.

5
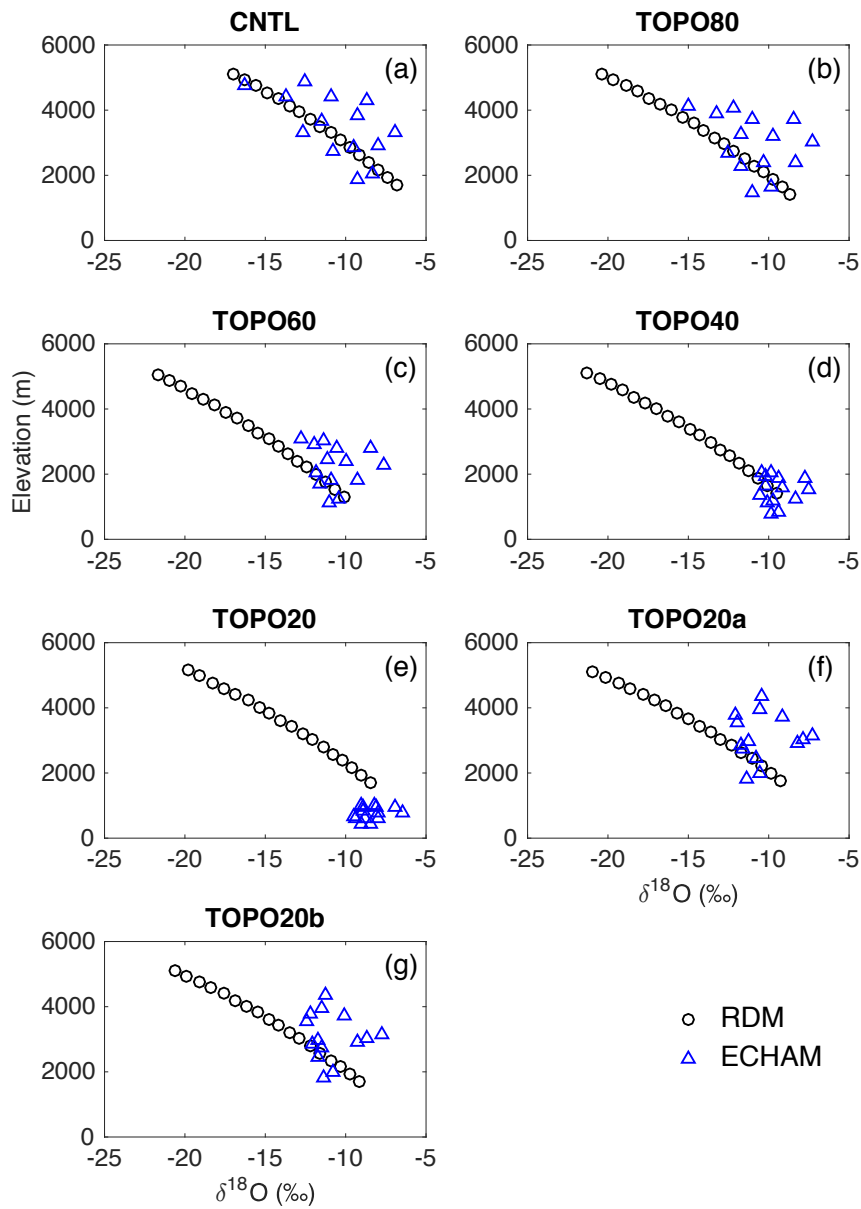
Figure S7. Same as figure S6 but for the transitional area between the western and the central part of the southern Himalayan flank.
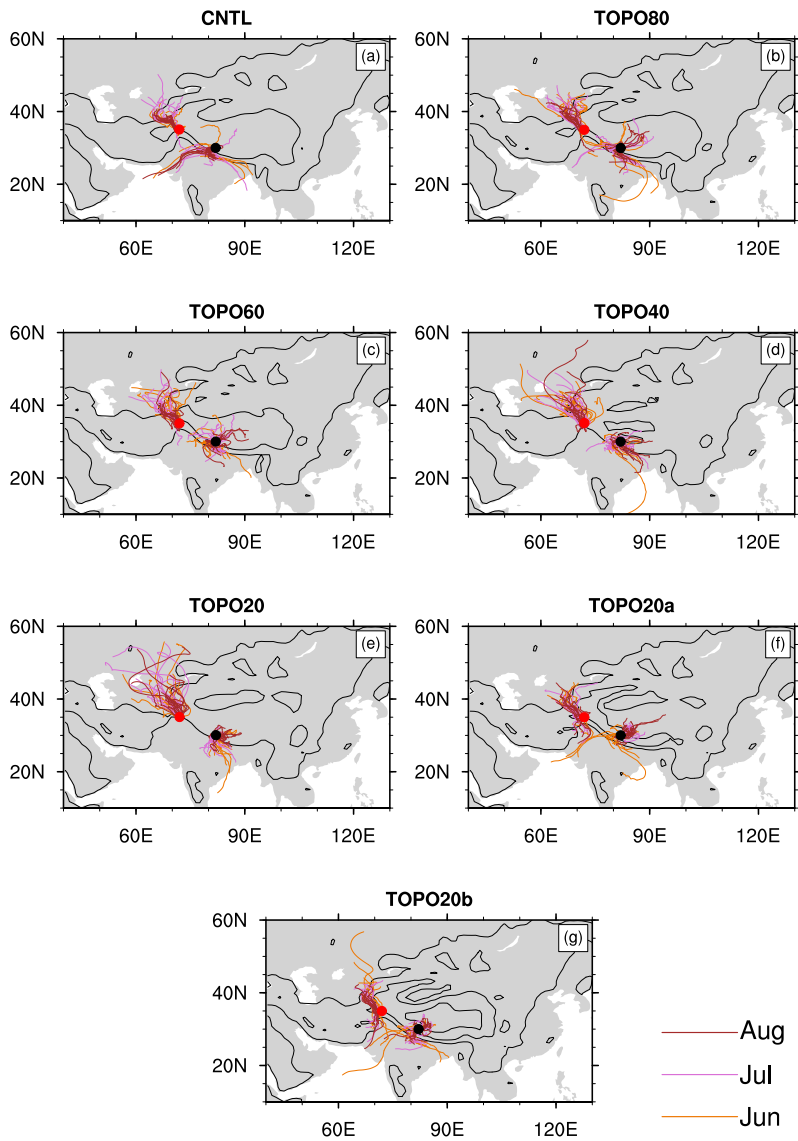
9

Figure S8. Back trajectory calculations for air parcels originating from the western (35° N, 72° E, red filled circle) and transitional (30° N, 82° E, black filled circle) regions for (a) CNTL, (b) TOPO80, (c) TOPO60, (d) TOPO40, (e) TOPO20, (f) TOPO20a, and (g) TOPO20b cases. Black contour lines show 500 and 2000 m Tibetan surface elevations. In each case, 42 trajectories were estimated, one each for June, July, and August for 14 years. Line colors represent the month. As seen from this figure, moisture sources for the transitional region in high-elevation scenarios come from both the Bay of Bengal and the Arabian Sea. In comparison, the sources of the monsoonal regions come primary from the Bay of Bengal and northwest India (not shown).
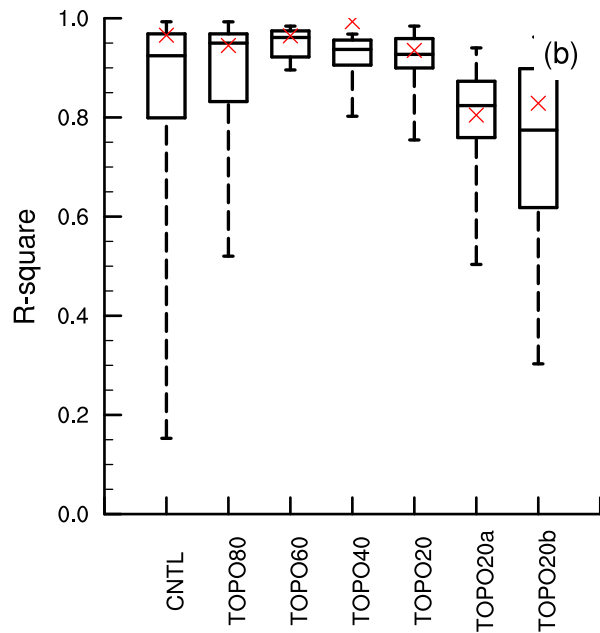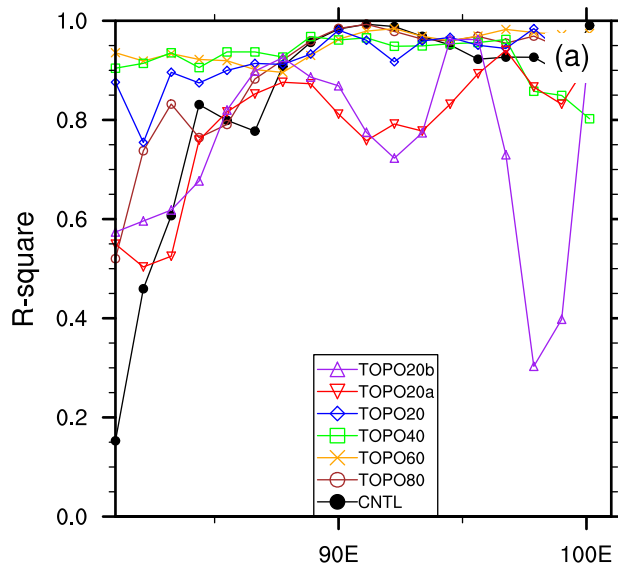
Figure S9. (a) The r-squared indicating goodness of fit of the regression in Fig 11. (b) Box plots showing minimum, maximum, median, and quartile values for (a). Red "x" represents the mean values for each scenario, calculated by regressing longitudinally averaged δ¹⁸Oₚ across the Tibetan Plateau to latitude.
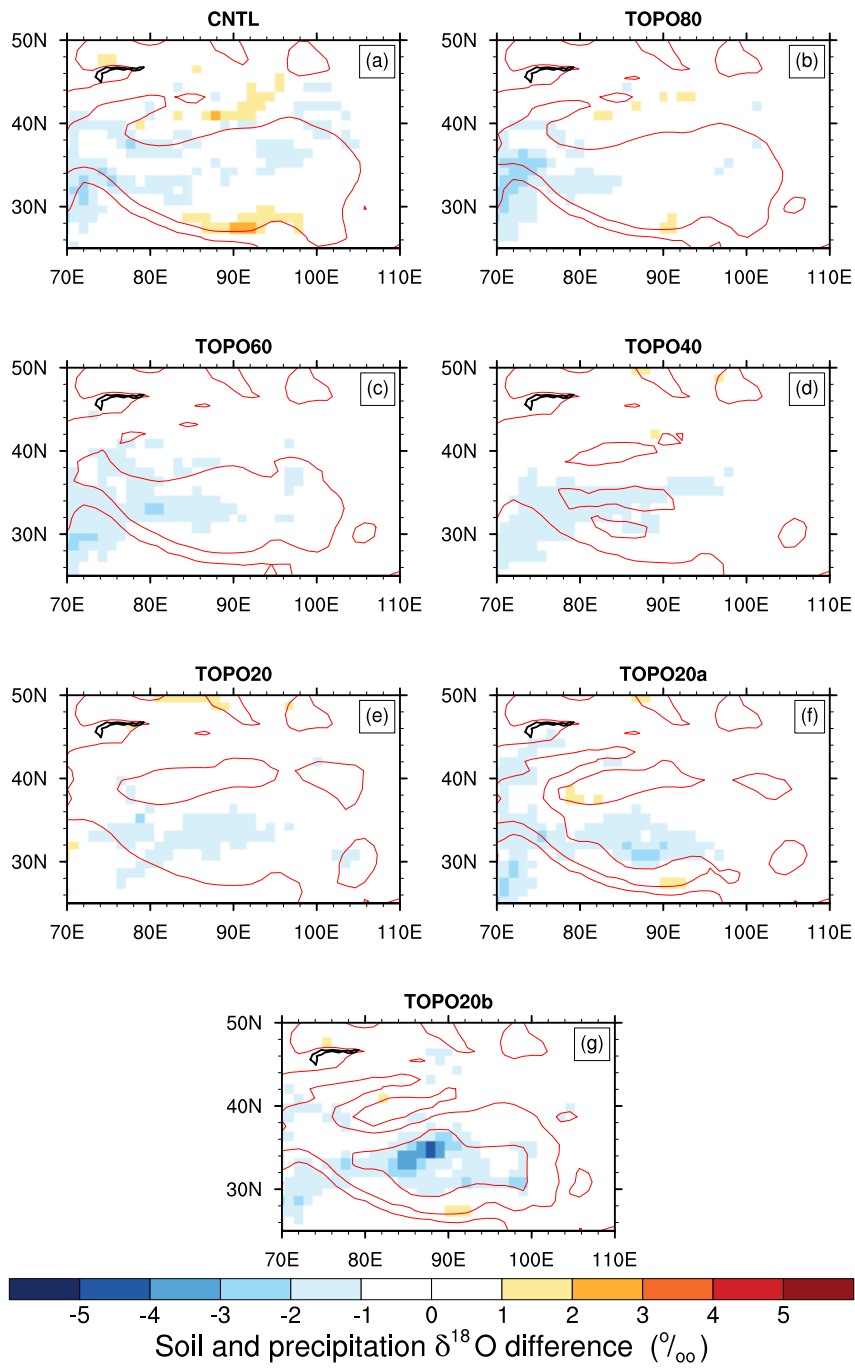
5

Figure S10. Simulated summer soil $\delta^{18}O$ minus precipitation $\delta^{18}O$ for each case (a) CNTL, (b) TOPO80, (c) TOPO60, (d) TOPO40, (e) TOPO20, (f) TOPO20a, and (g) TOPO20b. The soil and precipitation $\delta^{18}O$ values are quite similar on the plateau, with soil $\delta^{18}O$ slightly lower than that in precipitation.
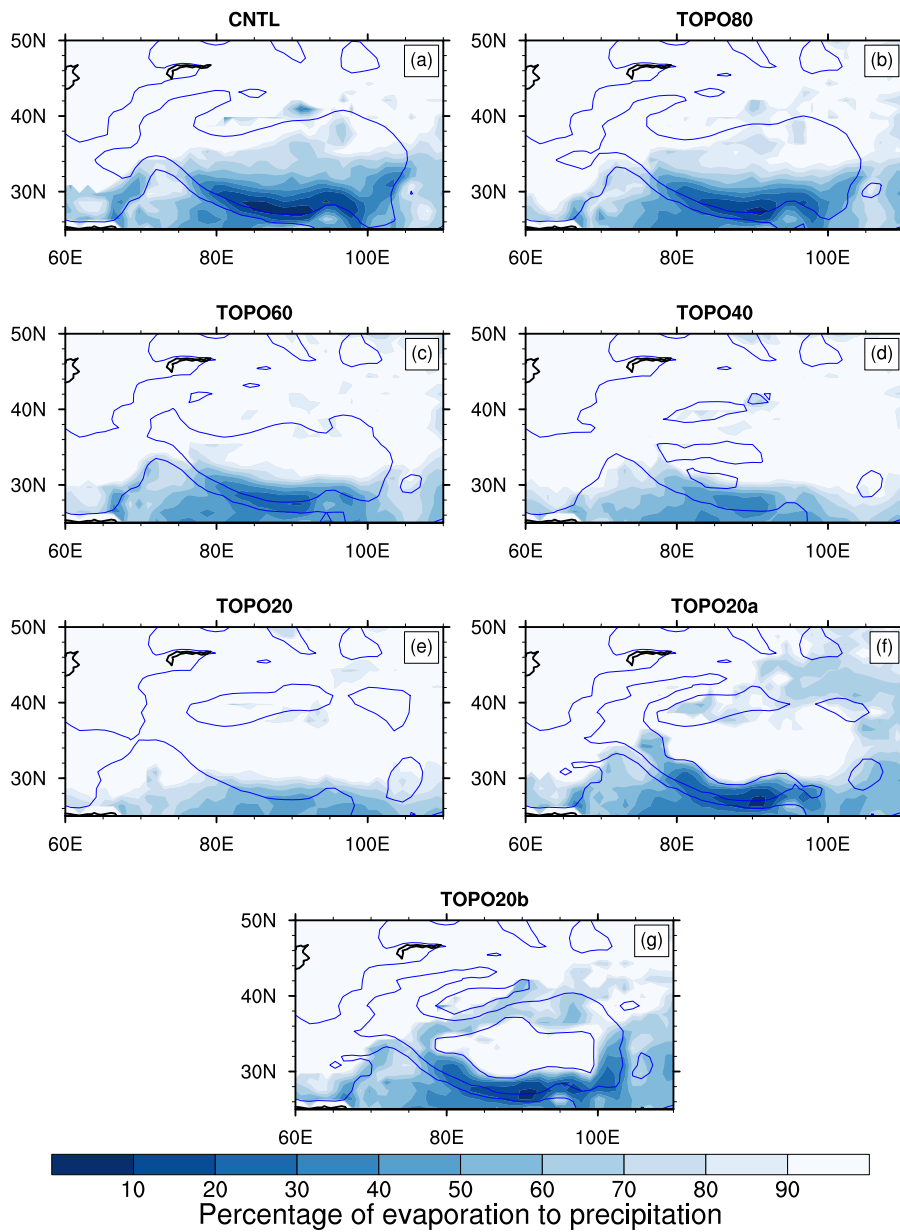
5

Figure S11. Fraction of summer land surface evaporation to total summer precipitation (shaded) for the (a) CNTL, (b) TOPO80, (c) TOPO60, (d) TOPO40, (e) TOPO20, (f) TOPO20a, and (g) TOPO20b cases. Blue contour lines mark the 500 and 2000 m Tibetan surface elevations. Larger portion of total precipitation is evaporated as the elevations are reduced.
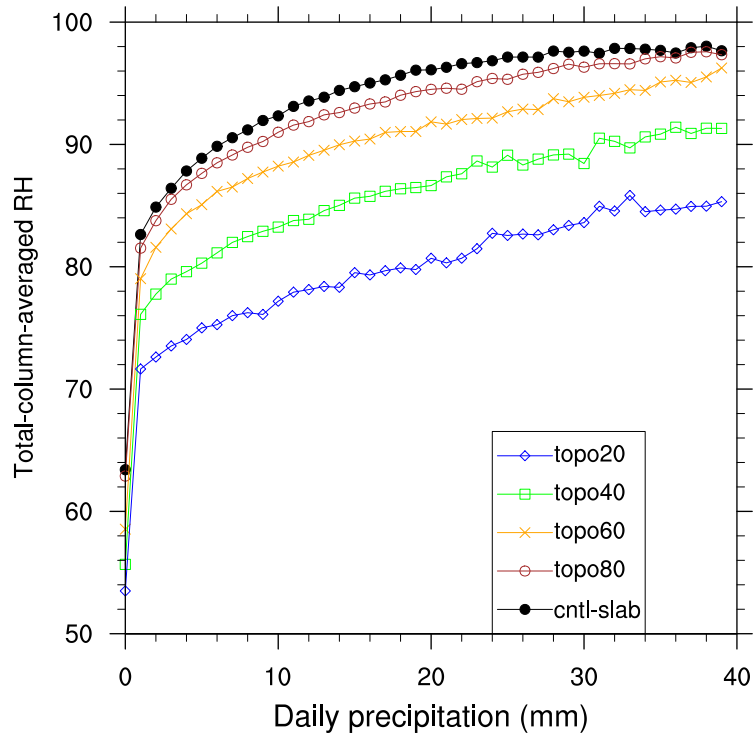
5

Figure S12. ECHAM5 total-column-averaged relative humidity (%) versus daily precipitation rate (mm day^{-1}) for the Tibetan plateau. RH is higher in high-elevation scenarios than that in low-elevation scenarios at any given precipitation rate.
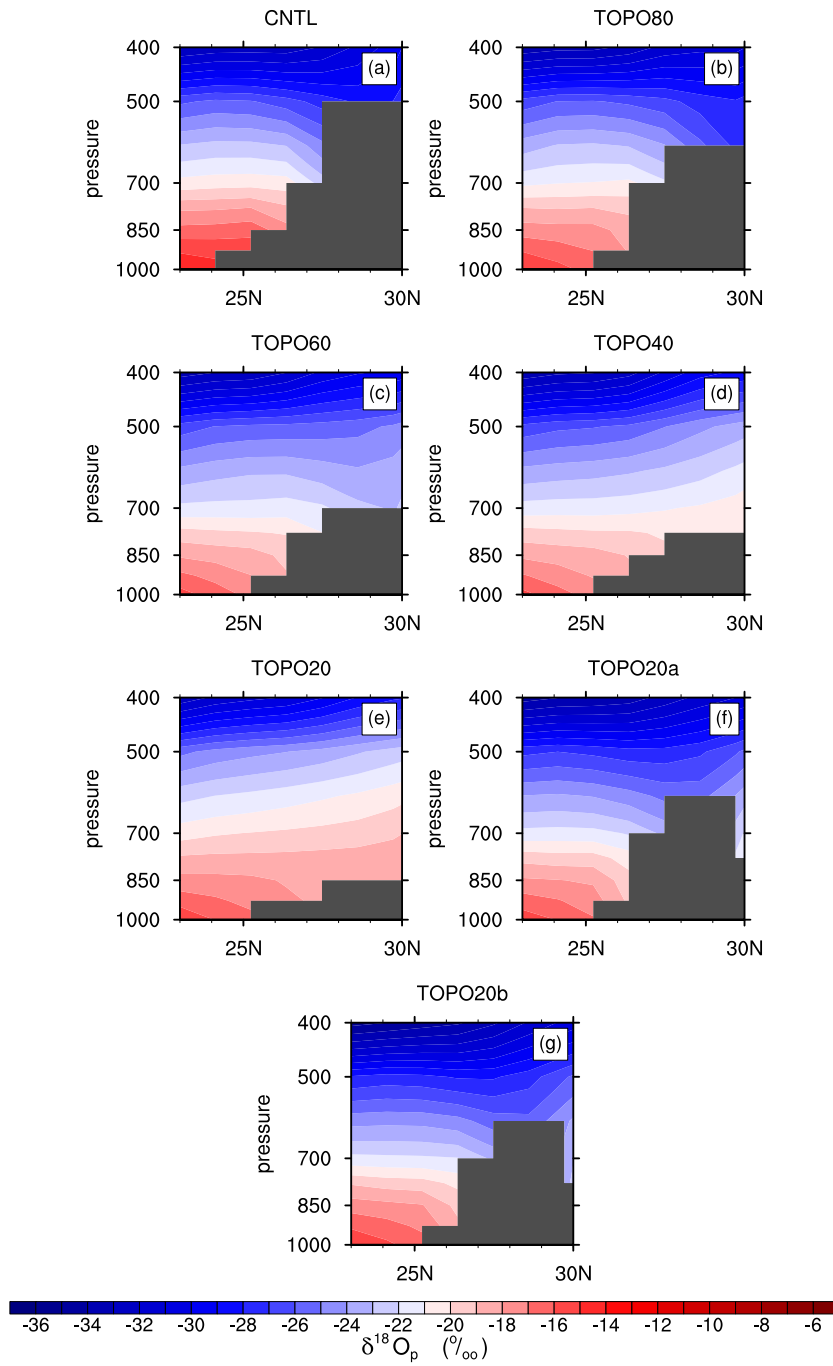
Figure S13. Vertical profile of air $\delta^{18}O$ along the longitudinal section of 90°E for the (a) CNTL, (b) TOPO80, (c) TOPO60, (d) TOPO40, (e) TOPO20, (f) TOPO20a, and (g) TOPO20b cases. Gray shading denotes raised topography (i.e., mountains). The low-level (~26° N) $\delta^{18}O_v$ is more depleted in lower-elevation scenarios than in CNTL. Abe, M., Kitoh, A., and Yasunari, T.: An Evolution of the Asian Summer Monsoon Associated with Mountain Uplift—Simulation with the MRI Atmosphere-Ocean Coupled GCM—, Journal of the Meteorological Society of Japan. Ser. II, 81, 909-933, doi:10.2151/jmsj.81.909, 2003.